Non-linear Approach for MRI to intra-operative US Registration Using Structural Skeleton

Jisu Hong[1] and Hyunjin Park[2,3]([✉])

[1] Department of Electronic, Electrical and Computer Engineering,
Sungkyunkwan University, Suwon, Korea
bal25ne@skku.edu
[2] School of Electronic Electrical Engineering,
Sungkyunkwan University, Suwon, Korea
hyunjinp@skku.edu
[3] Center for Neuroscience Imaging Research (CNIR),
Institute for Basic Science, Suwon, Korea

Abstract. Gliomas are primary brain tumors of central nervous system. Appropriate resection of gliomas in the early tumor stage is known to increase survival rate. However, the accurate resection of tumor is a challenging problem because the soft tissue shift may occur during the operation. To provide proper guidance to neurosurgery, it is necessary to align magnetic resonance imaging (MRI) and intra-operative ultrasound (iUS). In previous studies, many algorithms tried to find fiducial points that can lead to the appropriate registration. But these methods required manual specifications from experts to ensure the reliability of the fiducials. In this study, we proposed a data-driven approach for MRI-iUS non-linear registration using structural skeletons. The visualization of our results indicated that our approach might provide better registration performance.

Keywords: MRI · intra-operative US · Registration · Skeleton

1 Introduction

Gliomas are primary brain tumors of central nervous system (CNS) [1]. The gliomas arise from the glia which supports the CNS and can permeate to the neighboring areas. They can be categorized in grade from I to IV based on their histological characteristics defined by the World Health Organization (WHO) [2]. The grade I and II gliomas are classified as low-grade gliomas (LGG) and grade III and IV gliomas are classified as high-grade gliomas (HGG). The LGG grow comparatively slowly but due to their infiltrative attribute and threatening behavior, the mean 10-year survival is 30% [1]. It is generally accepted that the resection of the LGG may increase the survival rate [3].

Intra-operative ultrasound (iUS) was first proposed as a potential tool for guiding resection of intracranial tumors in 1980 [4]. The iUS is still generally used because it enables the surgeons to track the brain tissues and surgical tools in a fast, inexpensive, and real-time way. In addition, the gliomas can often be detected in iUS images even

when they are not detectable under the microscope. This can promote accurate resection and helps to obtain better surgical results. However, it is difficult to design effective surgical plans without the high-quality image-guidance. One of the principal reason is that the surgical target and the other tissues can be shifted by intra-operative factors such as tissue removal, change of intracranial pressure and drug administration. However, these shifts may not be easily observed in the surgeon's field of view.

To estimate and rectify for spatial errors resulting from intra-operative brain shifts, registration of pre-operative magnetic resonance imaging (MRI) to iUS image has been suggested [5–7]. This approach helps updating the surgical plans under the continuous brain tissue shift in contrast to comparing directly between pre- and intra-operative images. Many algorithms for registration have been proposed in the past years. However, it is technically demanding because of its intrinsic limits such as the differences between modalities and image qualities. Because of these problems, most MRI to iUS registration methods were conducted by using manually selected fiducial points.

In this paper, we proposed an automatic non-linear MRI-iUS registration algorithm using structural skeletons. First, we conducted several pre-processing steps on the MRI and iUS. Then we calculated the structural skeletons of both modalities. Finally, we calculated the displacement fields using the pairs of skeleton for the MRI-iUS registration.

2 Materials and Methods

2.1 Dataset

As this proposal is submitted to the CURIOUS 2018 challenge, we used the Retrospective Evaluation of Cerebral Tumors (RESECT) dataset [8]. The dataset includes pre-operative 3T MRI images including Gadolinium-enhanced T1w and T2 FLAIR scans, iUS images as a 3D volume covering the entire tumor region after craniotomy but before dura opening and the expert-labeled homologous anatomical landmarks, defined on all image modalities. All reconstructed images were acquired from the same subject and were spatially aligned under the same world coordinate space.

The MR protocol included T1w Gadolinium-enhanced sequence (TE = 2.96 ms, TR = 2000 ms, 192 slices, slice thickness = 1 mm, acquisition matrix = 256 × 256, in-plane resolution = 1.0 × 1.0 mm^2) and FLAIR sequence (TE = 388 ms, TR = 5000 ms, 192 slices, slice thickness = 1 mm, acquisition matrix = 256 × 256, in-plane resolution = 1.0 × 1.0 mm^2), acquired on a 3T MRI scanner with a 20-channel head coil. For subject 2, 14, 15 (Case 2, 14, 15), the pre-operative MRI included T1w sequence (TE = 2.3 ms, TR = 2500 ms, 176 slices, slice thickness = 1 mm, acquisition matrix = 512 × 496, in-plane resolution = 1.0 × 1.0 mm^2) and FLAIR sequence (TE = 333 ms, TR = 6000 ms, 176 slices, slice thickness = 1 mm, acquisition matrix = 256 × 224, in-plane resolution = 1.0 × 1.0 mm^2) acquired on a 1.5T MRI scanner with a 12-channel head coil.

The iUS images were acquired using the Sonowand Invite neuronavigation system. In most cases, the 12FLA-L linear probe with a frequency range of 6 to 12 MHz and a

footprint of 48×13 mm^2 was used. For smaller tumors, the 12FLA flat linear array probe with a frequency range of 6 to 12 MHz and a footprint of 32×11 mm^2 was used. The resolution of reconstructed 3D volume varied from $0.14 \times 0.14 \times 0.14$ mm^3 to $0.24 \times 0.24 \times 0.24$ mm^3 depending on the probe types and imaging depth.

2.2   MRI Pre-processing

First, we corrected non-uniformity to remove field bias from the MRI image. After the bias removal, we obtained the masks of grey matter (GM), white matter (WM) and cerebrospinal fluid (CSF) from the T1w image. After that, we cropped the T1w image and its masks to match with the location and size of iUS image. Then we resampled the cropped image and masks into $0.2 \times 0.2 \times 0.2$ mm^3 voxel resolution. Because the intensity distribution of iUS image was well matched with the GM and CSF mask from the MRI image, we used the inversed WM mask instead of using the summation of GM and CSF mask. The small hole of the inversed mask was removed using flood-fill algorithm with connectivity parameter 4 per each z-slice. The output mask was used to calculate the structural skeleton of MRI image.

2.3   iUS Pre-processing

We resampled the iUS image using the cropped and resampled T1w image as reference. As the voxel resolution of reference image was $0.2 \times 0.2 \times 0.2$ mm^3, the iUS image resampled to the same resolution. The order of axis in iUS image was matched with the reference image. Then, the resampled iUS image was blurred with 0.5 mm full width at half maximum (FWHM) Gaussian kernel and filtered with $3 \times 3 \times 3$ median kernel under voxel coordinate space. A binary mask image was obtained by applying threshold to the filtered image and was dilated by the ball shaped structure elements with voxel radius 15. The dilated mask was used for calculating the skeleton. We used a semi-automatic intensity-based segmentation algorithm to compute the binary masks for both MRI and iUS. The masks were structurally enhanced using preprocessing steps such as full with half maximum smoothing and morphological operations, which was performed with typical hyperparameters.

2.4   Structural Skeleton

After the refinement of the binary masks, the Euclidean skeletons were calculated for both masks [9, 10]. For details, we inverted the masks and computed the Euclidean distance map. The ridges of the distance map were computed by watershed algorithm. The final skeletons of each masks were obtained by thresholding the gradient of the ridges.

2.5   Registration Using Deformation Fields

We applied the Demon's algorithm for non-linear registration [11]. This algorithm performed over the entire space of displacement field. At first, a spatial transformation field was initialized. Then, we iterated the following steps until the error converged:

(1) Given field s, compute a correspondence update field u by minimizing the error E which can be defined as following Eq. (1).

$$E(u) = ||F - M \cdot (s + u)||^2 + \left(\frac{\sigma_i}{\sigma_x}\right)||u||^2 \qquad (1)$$

(2) Let c as $s + u$.
(3) Use diffusion-like regularization by conducting the Gaussian smoothing to the accumulated transformation field c
(4) Substitute s with the filtered c.

As mentioned above, the variable s accounts for the given spatial transformation field and u for the corresponding update field. The variable F accounts for the fixed iUS image, M for the moving MRI image, σ_i for the noise on the image intensity and σ_x for a spatial uncertainty on the correspondences.

2.6   Mean Target Registration Error

We measured the Euclidean distances between the MRI landmarks after the registration and the corresponding iUS landmarks to calculate the target registration errors (TREs). All landmarks were averaged per each case.

3   Results

3.1   Crop and Resampling

Figure 1 shows the results images after cropping and resampling. Figure 1(a) and (b) represent the T1w image and the iUS image respectively. Both images were well aligned to each other so that they could be used for the following processes.

3.2   Estimated Skeleton

Cropped and resampled MRI and iUS images were used to calculate their structural skeletons. Figure 2 shows the skeletons obtained from the MRI and iUS images. Figure 2(a) shows the MRI image and its skeleton, and Fig. 2(b) shows the iUS image and its skeleton.

3.3   Skeleton Registration Using Displacement Fields

Figure 3 shows the results of the registration using the Demon's deformation algorithm. Figure 3(a) shows the original skeleton of the MRI image. Figure 3(b) and
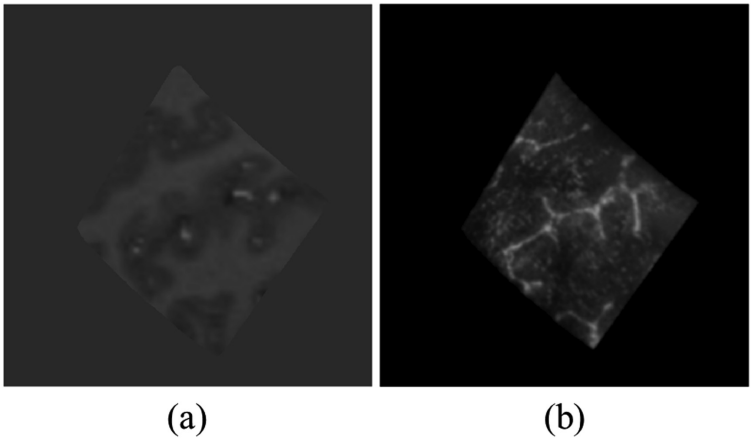
Fig. 1. The MRI image and iUS image obtained after crop and resampling of case 1. (a) is the MRI image and (b) is the iUS image.
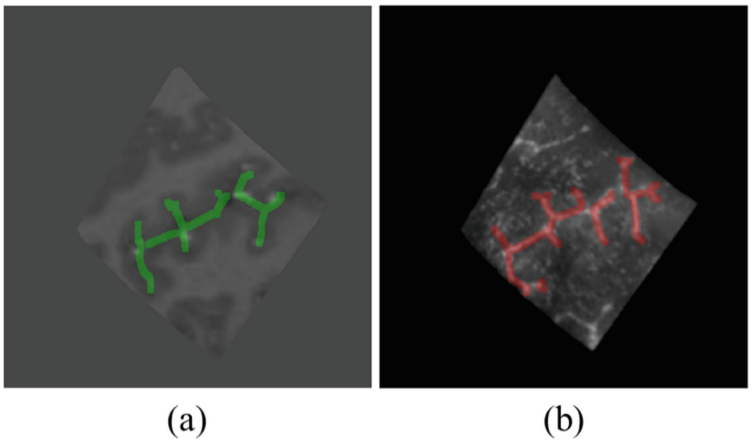

Fig. 2. The MRI image and iUS image of case 1 with their structural skeleton. (a) The structural skeleton of the MRI was indicated with green line and (b) the structural skeleton of the iUS was indicated with red line. (Color figure online)

(c) represents the deformation fields along x-axis, top-to-bottom axis in this image, and y-axis, left-to-right axis in this image respectively. The deformation field along z-axis was also calculated but it was not shown in this figure for better visualization. Figure 3 (d) is the skeleton of the MRI image after the registration to iUS image. We compared these results with the original iUS image and its skeleton (Fig. 4). The skeleton of the iUS image was shown as the structural line with red color on both Fig. 4(a) and (b). The structural line with green color on Fig. 4(a) represents the skeleton of MRI image before the registration and the same line on Fig. 4(b) represents the skeleton after the registration.
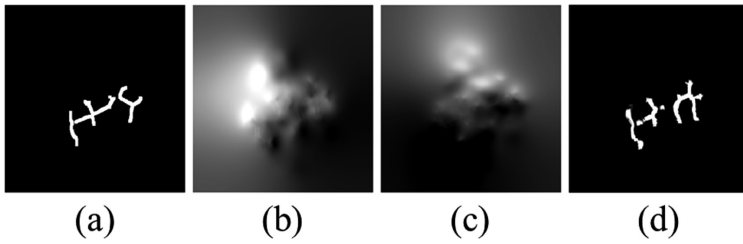
Fig. 3. The results of the registration using the Demon's deformation algorithm. (a) is the original skeleton of MRI. (b) and (c) shows the displacement field estimated after the registration on the x-axis and the y-axis respectively. (d) is the skeleton of MRI after the MRI-iUS registration.
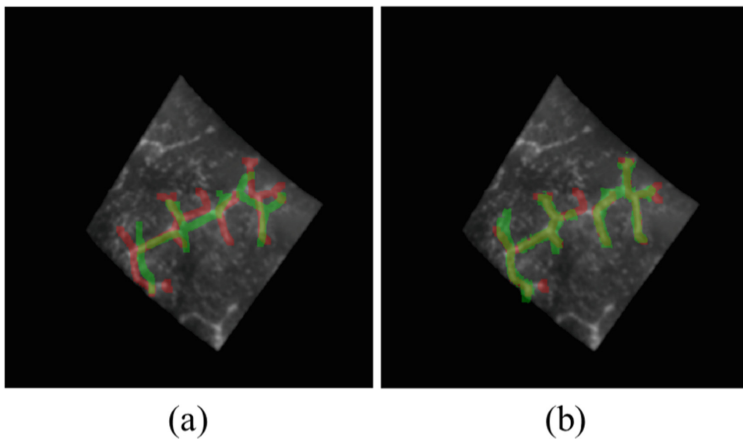

Fig. 4. The demonstration of the registration using skeletons overlapped on the same iUS image of case 1. (a) shows the skeleton of original MRI with red line and the skeleton of iUS image with green line. (b) shows the skeleton of registered MRI with red line and the skeleton of iUS image with green line. (Color figure online)

3.4   Image Registration Using Estimated Fields

As we calculated the deformation fields at each location on every axis, we could obtain the final registered MRI image (Fig. 5). Figure 5(a) shows the original MRI image overlapped with the iUS image. The MRI image was visualized with the green color and the iUS image was visualized with red color. Figure 5(b) shows the registered MRI image overlapped with the iUS image.

3.5   Landmark Evaluation

The Euclidean distances between two corresponding landmarks were measured. Then, the mTREs of all cases were measured to evaluate the results (Table 1).
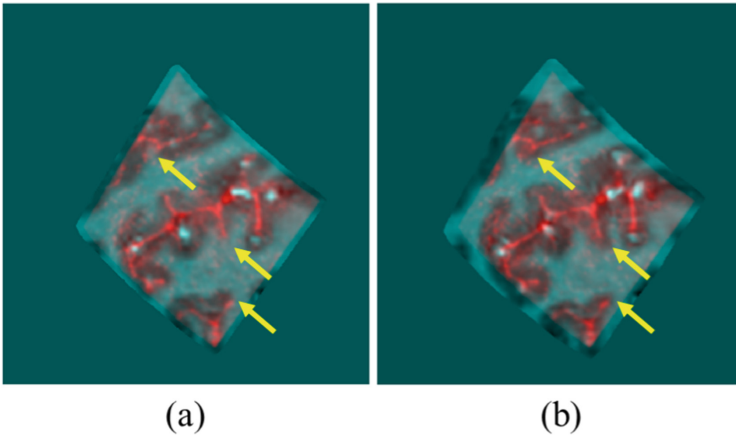
(a)   (b)

Fig. 5. The demonstration of the registration. (a) The MRI image before the registration was shown as green and the original iUS image was shown as red. (b) The MRI image after the registration was shown as green and the original iUS was shown as red. (Color figure online)

Table 1. The mean target registration error for the all 22 cases.

Case	Mean target before-registration error (mm)	Mean target after-registration error (mm)
1	1.8196	3.1779
2	5.6755	5.8900
3	9.5772	9.6980
4	2.9859	3.9038
5	12.0191	11.7075
6	3.2696	2.4846
7	1.8190	3.3739
8	2.6344	3.3612
12	19.6793	17.9112
13	4.5716	3.9380
14	3.0322	3.3116
15	3.2115	5.0273
16	3.3909	3.3728
17	6.3939	7.7679
18	3.5604	3.5396
19	3.2805	4.0459
21	4.5463	3.5659
23	7.1108	5.9944
24	1.1011	1.7430
25	10.0601	11.6948
26	2.8339	2.1951
27	5.7560	5.5233
Mean ± SD	5.38 ± 4.27	5.60 ± 3.94

References

1. Shields, L.: Management of low-grade gliomas: a review of patient-perceived quality of life and neurocognitive outcome. World Neurosurg. **87**(1–2), 299–309 (2014)
2. Louis, D.N.: The 2016 World Health Organization classification of tumors of the Central Nervous System: a summary. Acta Neuropathol. **131**(6), 803–820 (2016)
3. Asgeir, S.: Comparison of a strategy favoring early surgical resection vs a strategy favoring watchful waiting in low-grade gliomas. JAMA **308**(18), 1881–1888 (2012)
4. Voorhies, R.M.: Preliminary experience with intraoperative ultrasonographic localization of brain tumors. Radiol. Nucl. Med. **10**, 8–9 (1980)
5. Hill, D.L.: Medical image registration. Phys. Med. Biol. **46**(3), R1–R45 (2001)
6. Sotiras, A.: Deformable medical image registration: a survey. IEEE Trans. Med. Imaging **32**, 1153–1190 (2013)
7. Schnabel, J.A.: Advances and challenges in deformable image registration: from image fusion to complex motion modelling. Med. Image Anal. **33**, 145–148 (2016)
8. Xiao, Y.: REtroSpective Evaluation of Cerebral Tumors (RESECT): a clinical database of pre-operative MRI and intra-operative ultrasound in low-grade glioma surgeries. Med. Phys. **44**(7), 3875–3882 (2017)
9. Couprie, M.: Topological maps and robust hierarchical Euclidean skeletons in cubical complexes. Comput. Vis. Image Underst. **117**(4), 355–369 (2013)
10. Telea, A.: An augmented fast marching method for computing skeletons and centerlines. In: Proceedings of the symposium on Data Visualization, pp. 251–259. Eurographics, Aire-la-Ville (2002)
11. Vercauteren, T., Pennec, X., Perchant, A., Ayache, N.: Non-parametric diffeomorphic image registration with the demons algorithm. In: Ayache, N., Ourselin, S., Maeder, A. (eds.) MICCAI 2007. LNCS, vol. 4792, pp. 319–326. Springer, Heidelberg (2007). https://doi.org/10.1007/978-3-540-75759-7_39